Calculation of Transonic Flow around Axisymmetric Inlets

B. G. Arlinger*
Aerospace Division, SAAB-SCANIA AB, Linköping, Sweden

The transonic flow around an axisymmetric inlet is calculated for a prescribed mass-flow ratio. The inlet consists of an initial part of arbitrary geometry, which is continued to downstream infinity as a straight, circular tube. With a sequence of conformal mappings and a final coordinate stretching, the whole exterior and interior flowfield is mapped to a rectangular domain in which the full inviscid transonic potential equation is solved using type-dependent line-relaxation. Comparisons of calculated pressure distributions are made with experimental results for various inlets and Mach numbers from 0.5 to 0.95 yielding very good agreement.

I. Introduction

In recent years a great effort has been devoted to the design of transonic airfoils and wings. Several efficient computer programs for analysis and design are in use today, especially for airfoils.

For engine inlet analysis, however, still only a few programs exist dealing with transonic flow. Partly, this may be due to the more complex geometry involved. This fact has favored other approaches to the analysis problem than in the airfoil case. Keith et al.[1] thus apply a streamtube curvature technique and Grossman and Moretti[2] use a time-dependent approach. In the latter work and to some extent also in the former, certain numerical problems seem to develop when approaching high subsonic Mach numbers, yielding unsatisfactory pressure distributions. Colehour[3] uses the type-dependent line-relaxation technique, which has been successful for the airfoil cases since it was introduced by Murman and Cole.[4] As coordinate system Colehour uses the incompressible streamlines and potential lines, which, in effect, results in fixing the compressible stagnation point at the same location as the incompressible stagnation point.

The present method uses a mapping which does not introduce any singular point within the finite part of the flowfield. Conformal mapping technique is used, yielding an orthogonal coordinate system in which the full inviscid equation for transonic potential flow is solved. The configuration studied is semi-infinite, being continued to downstream infinity as a straight, circular tube. The equation is solved for specified mass-flow ratio using type-dependent line-relaxation. In regions of supersonic flow a so-called rotated difference scheme is used to get proper backward differencing independent of the angles between the velocity vector and the coordinate lines.

II. Basic Formulation

The configuration dealt with, as shown in Fig. 1, is axisymmetric and consists of a former part of arbitrary geometry which, after a prescribed length, is continued to downstream infinity as a straight, circular tube. The full inviscid transonic equation for the potential ϕ around the configuration is

$$(a^2-\phi_x{}^2)\,\phi_{xx}-2\phi_x\phi_r\phi_{xr}+(a^2-\phi_r{}^2)\,\phi_{rr}+a^2\,\frac{\phi_r}{r}=0 \qquad (1)$$

where x and r are coordinates aligned with and normal to the centerline, respectively. The sound velocity a is calculated from

$$a^2=a_\infty^2-[(\gamma-1)/2]\,(\phi_x^2+\phi_r^2-q_\infty^2)$$

with q denoting the velocity. The external and internal infinities are indicated by the subscripts ∞ and i, respectively. As boundary conditions are used:

$$\phi_n=0 \text{ along the inlet contour and along the centerline} \qquad (2a)$$

$$\phi\to q_\infty x \text{ when } x^2+r^2\to\infty \text{ outside the inlet} \qquad (2b)$$

$$\phi\to q_i x \text{ when } x\to\infty \text{ inside the inlet} \qquad (2c)$$

The internal downstream velocity q_i is calculated from the prescribed mass-flow ratio C_A, which in this paper is defined by the relation

$$C_A=A_\infty/A_i=(\rho_i/\rho_\infty)\,q_i/q_\infty \qquad (3)$$

where A denotes streamtube area (see Fig. 1), and ρ denotes density.

The advantage of using a potential formulation is great because only one unknown has to be used. The restriction to isentropic flow, which this means, is not very severe as long as the shock waves developing in the flow are weak.

To get simple and accurate expressions for the boundary conditions without any approximation to small perturbations, a new coordinate system has to be calculated having one coordinate line coinciding with the inlet contour and one coinciding with the centerline. This is achieved by using conformal mapping technique in several steps.

III. The Mapping

All the steps in the mapping are performed using analytic functions to get an orthogonal coordinate system with the scale factors depending on one single function, the mapping modulus. The basic principle when constructing the mapping is to transform the physical boundary contour (inlet contour + centerline) to a simple closed contour and then transform to a circle using a Fourier series. Finally, the circle contour is transformed to a rectangle using simple conformal mapping ended by a coordinate stretching.

A. Derivation of the Mapping

Denoting the physical plane by $z=x+ir$ a first transformation to a new plane, z_1 is made by inversion in a point z_* within the inlet contour, (Fig. 2).

Presented as Paper 75-80 at the AIAA 13th Aerospace Sciences Meeting, Pasadena, Calif., January 20-22, 1975; submitted February 6, 1975; revision received May 20, 1975.

Index categories: Subsonic and Transonic Flow; Aircraft Aerodynamics (Including Component Aerodynamics).

*Aerodynamic Research Engineer. Member AIAA.

$$z_1 = 2r_*/(z_* - z) \tag{4}$$

To separate the internal and external infinity points and thus open up the closed centerline in z_1 the square root function is used of $z_1 + i$ with a cut laid from the branch-point $z_1 = -i$, as marked in Fig. 2. The new transformation is

$$z_2 = i\sqrt{i(z_1 + i)} + 1 \tag{5}$$

and the flowfield boundary in this plane is seen in Fig. 3.

With the bilinear transformation

$$z_3 = iz_2/(z_2 - 2) \tag{6}$$

the internal infinity point $z_2 = 2$ is brought to infinity and the centerline to the positive real axis in the z_3-plane. When approaching the internal infinity the inlet inside contour in z_3 tends to a line with a constant positive imaginary part for increasing positive values of the real part. Thus, there is a possibility to "open up" the flowfield in the z_3-plane to get something like an upper half plane by using the exponential function

$$z_4 = \exp\ (c_3 z_3) \tag{7}$$

c_3 is a constant chosen so that

$$Im(\lim_{z_3 \to \infty} c_3 z_3) = \pi \tag{8}$$

for z_3 on the inlet inside contour, yielding the value

$$c_3 = (\pi/2) r_*/r_i$$

where r_i denotes the internal radius far downstream in the inlet. The flowfield contour in the z_4-plane, see Fig. 4, is now easily transformed to a simple closed contour without corners using

$$z_5 = -[z_4 - (1 + i\,b_4)]/[z_4 - (1 - ib_4)] \tag{9}$$

with the constant b_4 set equal to some suitable value, usually between 0.1 and 1.

The contour in the $z_5$plane (Fig. 4) has a continuously varying slope but curvature singularities in the two infinity points. This fact requires some consideration before mapping to a circle using a Fourier series.

Because the exponential function was used in the transformation to z_4, the far downstream region inside the inlet is very densely compressed around the internal infinity point in z_5. This means that the Fourier series mapping of this region will fail to give high accuracy in the mapping functions sufficiently near the internal infinity. The solution to this problem is to use a simple Taylor series expansion for the mapping functions close to this point. Because the leading terms of that series do not contain the curvature in the internal infinity point, the curvature singularity here is of minor importance. Further comments on the Fourier series mapping close to $z_5 = -1$ are given in Sec. III B.

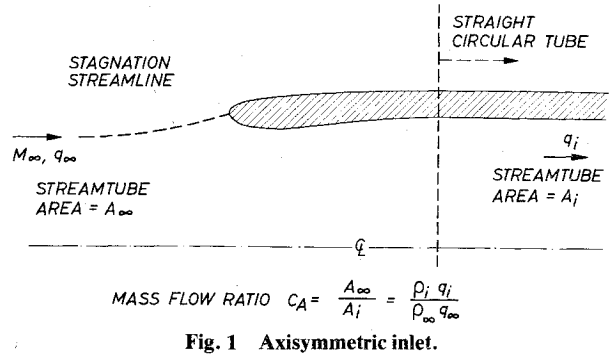

Fig. 1 Axisymmetric inlet.

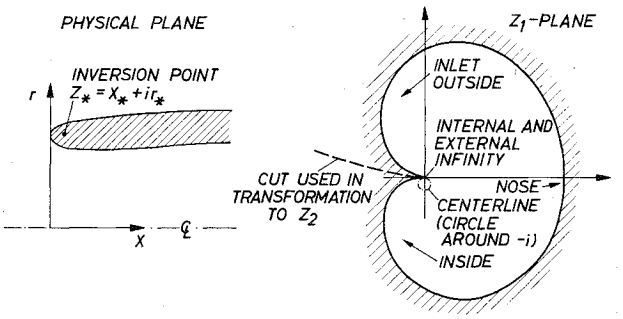

Fig. 2 The transformation $z \to z_1$.

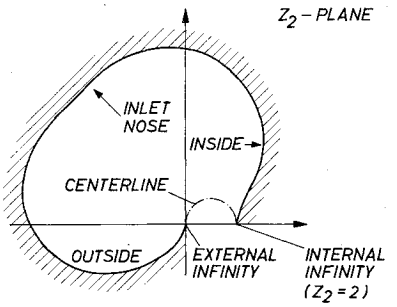

Fig. 3 The contour in the z_2-plane.

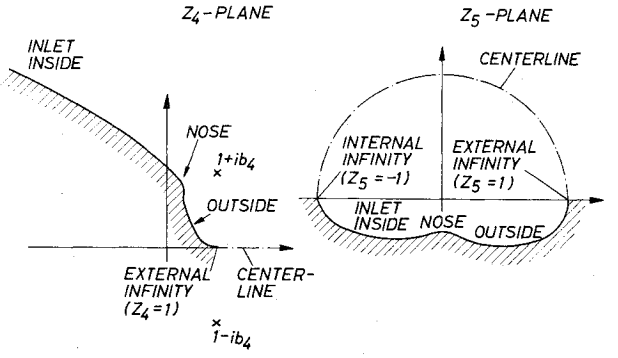

Fig. 4 The contour in the z_4- and z_5-planes.

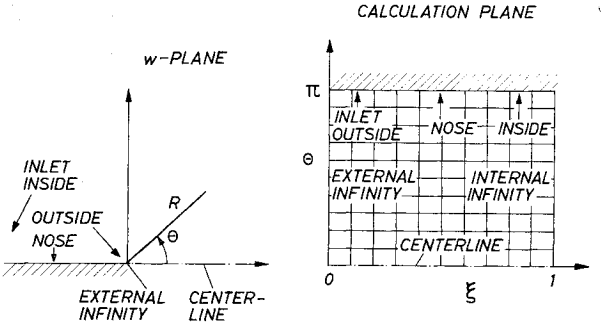

Fig. 5 The w-plane and the calculation plane.

At the external infinity point $z_5 = 1$, the curvature has a finite discontinuity. This singularity must be properly accounted for when calculating the behavior of z near the external infinity, to get correct asymptotic expressions for the potential in this region. The best way of handling this is to find a transformation which removes the curvature singularity in $z_5 = 1$ before the transformation to a circle is performed. A study reveals that the transformation should be of the type

$$z_5 \sim z_6[1 + c_6(z_6 - 1)^2 \ln(z_6 - 1)]$$

where the constant c_6 has the value

$$c_6 = -i2\, b_4 r_i r_e / \pi^2 r_*{}^2 \tag{10}$$

with r_e and r_i denoting the external and internal radius of the downstream constant geometry part of the inlet.

To get a single-valued mapping of the z_5 flowfield and a contour in the z_6-plane which differs only slightly from that in the z_5-plane, the transformation used in the mapping procedure was

$$z_5 = z_6 \left\{ 1 + c_6 \frac{(z_6-1)^2 [\ln(z_6-1) - i\pi/2]}{1 - i\, a_6 c_6 (z_6-1)} \right\} \tag{11}$$

where the constant a_6 was given some value above about 5. The transformation to a unit circle was made next using the relation

$$z_6 - z_6{}^* = z_7 \exp\left[\sum_{n=0}^{M} (\alpha_n + i\,\beta_n) z_7^n \right] \tag{12}$$

with the point $z_6{}^*$ usually located close to or in $z_6 = 0$. With the external infinity point located in $z_7 = 1$ the internal infinity point will map to some point denoted by $z_7 = \exp(i\varphi_7)$. By the bilinear transformation

$$w = -\exp(i\varphi_7/2)\,(z_7 - 1)/[z_7 - \exp(i\varphi_7)] \tag{13}$$

the flowfield inside the unit circle is finally mapped on the upper half plane (Fig. 5).

To get a finite computation space and the same scale factors for distances along the inside and outside inlet contour for large values of $Re(z)$, the radius R in $w = Re^{i\theta}$ is transformed by the relation

$$R = \exp[\xi/(1-\xi)] - 1 \tag{14}$$

Regarding the $\xi - \theta$-plane, the flowfield is thus mapped to the rectangle $0 \le \xi \le 1, 0 \le \theta \le \pi$ (Fig. 5). A simple rectangular coordinate mesh of constant meshsize is used in this plane for solving the finite difference form of the potential equation. The corresponding coordinate mesh in the physical plane is illustrated in Fig. 6.

The mapping functions which have to be calculated in the $\xi - \theta$-plane for use in the transformed potential equation are the mapping modulus B and the radius r

$$B = |dz/dw|$$

$$r = im(z)$$

When studying the behavior of these functions and the potential near the two infinity points the corresponding asymptotic expressions for z is needed. Written as functions of w they are

$$w \to 0 \quad z = -C_2/w + C_3 \ln w + 0(1) \tag{15a}$$

$$w \to \infty \quad z = C_1 \ln w + \text{const} + C_4/\ln w + 0[1/(\ln w)^2] \tag{15b}$$

with the four constants

$$C_1 = r_i/\pi \tag{16a}$$

$$C_2 = \frac{r_* c_3 a_4}{2 b_4 D_1 \sin(\varphi_7/2)} \left(1 + \frac{a_3}{b_3{}^2} \right) \tag{16b}$$

$$C_3 = r_e/\pi \tag{16c}$$

$$C_4 = (r_* c_3/2)\,(a_3 - 1) \tag{16d}$$

where

$$D_1 = (dz_6/dz_7)_{z_7=1}$$

and a_3, b_3 and a_4 are defined in connection with Eq. (18).

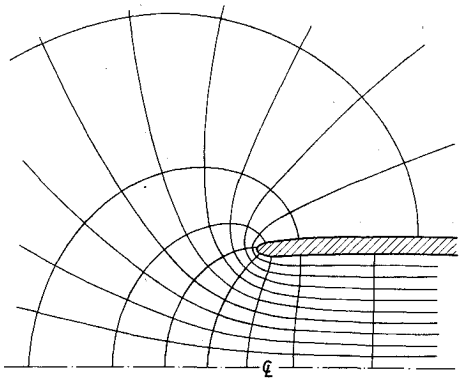

Fig. 6 The coordinate mesh in the physical plane.

B. Some Numerical Aspects on the Mapping

The numerical computation of the Fourier coefficients in Eq. (12) is made in an iterative sequence, first taking the complex logarithm of both sides. Fast Fourier transformations are used in a way similar to Jameson,[5] which renders the computation very fast. When evaluating B the derivative dz_6/dz_7 is needed, which is calculated using the expresssion

$$\frac{dz_6}{dz_7} = \exp\left[\sum_{n=0}^{M} (\gamma_n + i\delta_n) z_7{}^n \right] \tag{17}$$

in order not to decrease the numerical accuracy by differentiating Eq. (12). The use of length scale relations between z_6 and z_7 already calculated in the mapping [Eq. (12)] makes this derivative computation straightforward.

As already mentioned, the mapping functions calculated using the Fourier series transformations [Eqs. (12) and (17)] are inaccurate in the vicinity of the internal infinity. Instead of computing the Fourier series expressions, simple Taylor series expansions around $\xi = 1$ are used. The overlap between these mapping function expressions valid near $\xi = 1$ and those computed using the Fourier series relations may be improved by modifying the contour in the z_5-plane near $z_5 = -1$. Thus, if instead of z_3 the modified expression

$$z_3' = z_3 - a_3/(z_3 + b_3) \tag{18}$$

is used in Eq. (7) with properly chosen real positive constants a_3 and b_3, a z_5-contour will result, which is much "fuller" below the point $z_5 = -1$. Using the same number of Fourier terms the region around $z_5 = -1$ will now be more accurately mapped to the circle. If the mapping $z_3 \to z_3'$ is used, the Eqs. (9) and (10) should be changed to

$$z_5 = -[z_4 - (a_4 + i\, b_4)]/[z_4 - (a_4 - i\, b_4)] \tag{9a}$$

with

$$a_4 = \exp[-c_3 a_3/b_3]$$

and

$$c_6 = -i2\, b_4 r_i r_e / [\pi^2 r_*{}^2 a_4 (1 + a_3/b_3{}^2)] \tag{10a}$$

In most calculated examples nonzero values for a_3 were used, typical values ranging between 1 and 2.5 for a_3 and around 2 for b_3.

IV. Transformed Equations

The potential equation transformed to the coordinates R and θ in the w-plane may be written

$$(a^2-q_1^2)\phi_{RR}-2q_1q_2\frac{1}{R}\phi_{R\theta}+(a^2-q_2^2)\frac{1}{R^2}\phi_{\theta\theta}+a^2B\left(q_1\frac{r_R}{r}+\frac{q_2}{R}\frac{r_\theta}{r}\right)+B(a^2+q_2^2)\frac{q_1}{R}+(q_1^2+q_2^2)\left(q_1B_R+\frac{q_2}{R}B_\theta\right)=0 \tag{19}$$

with q_1 and q_2 denoting the velocity components in the R-and θ-directions, respectively.

$$q_1=(1/B)\phi_R \quad q_2=(1/RB)\phi_\theta \tag{20}$$

To make Eq. (19) suitable for numerical computation the coordinate stretching $\xi=\xi(R)$ according to Eq. (14) is first applied, and then all singularities at $\xi=0$ and 1 have to be subtracted or divided out. Thus, the following expression for the potential ϕ is introduced, based on the behavior of z for $\xi\to 0$ and $\xi\to 1$ derived from Eq. (15)

$$\phi(\xi,\theta)=C_1q_i\frac{\xi}{1-\xi}-C_2q_\infty\frac{\cos\theta}{\xi}+C_3q_\infty\ln\xi+\chi(\xi,\theta) \tag{21}$$

where $\chi(\xi,\theta)$ is a finite disturbance potential to be calculated. Introducing the nonsingular mapping functions

$$H=\xi^2\exp[\xi/(1-\xi)]B \tag{22a}$$

$$s=\xi r \tag{22b}$$

and using the shorthand notation E for $1-\exp[-\xi/(1-\xi)]$ yields the equation for the potential χ

$$(a^2-q_1^2)\xi^2(1-\xi)^4\chi_{\xi\xi}-2q_1q_2\frac{\xi^2(1-\xi)^2}{E}\chi_{\xi\theta}+(a^2-q_2^2)\frac{\xi^2}{E^2}\chi_{\theta\theta}+Q=0 \tag{23}$$

The expression for Q may be written

$$Q=Ha^2\left[q_1(1-\xi)^2\frac{\xi}{s}\left(\frac{s}{\xi}\right)_{|\xi}+\frac{q_2}{E}\frac{s_\theta}{s}\right]-(a^2-q_1^2)\frac{(1-\xi)^3}{\xi}\left[2C_2q_\infty\cos\theta+C_3q_\infty\xi(1+\xi)+2\xi^3\chi_\xi\right]+(a^2-q_2^2)\frac{\xi}{E^2}C_2q_\infty\cos\theta+(a^2+q_2^2)Hq_1\frac{1-E}{E}+\frac{2(1-\xi)^2}{E}q_1q_2C_2q_\infty\sin\theta+(q_1^2+q_2^2)\left[-2Hq_1\frac{(1-\xi)^2}{\xi}+H_\theta\frac{q_2}{E}+H_\xi(1-\xi)^2q_1\right] \tag{24}$$

The velocity components in the ξ-and θ-directions are

$$q_1=\frac{\xi^2(1-\xi)^2}{H}\left[C_1q_i\frac{1}{(1-\xi)^2}+C_2q_\infty\frac{\cos\theta}{\xi^2}+C_3q_\infty\frac{1}{\xi}+\chi_\xi\right] \tag{25a}$$

$$q_2=\frac{\xi^2}{HE}\left(C_2q_\infty\frac{\sin\theta}{\xi}+\chi_\theta\right) \tag{25b}$$

and the sound velocity a is calculated from

$$a^2=a_\infty^2-[(\gamma-1)/2](q_1^2+q_2^2-q_\infty^2)$$

The Equation (23) is to be solved using the boundary conditions $\chi_\theta=0$ for

$$\theta=\pi \quad 0\le\xi\le 1 \text{ (inlet contour)} \tag{26a}$$

$$\theta=0 \quad 0\le\xi\le 1 \text{ (centerline)} \tag{26b}$$

At the external and internal infinity, i.e., along the lines $\xi=0$ and $\xi=1$, $0\le\theta\le\pi$, the potential Eq. (23) attains the asymptotic forms

$$\xi=0 \quad (1-M_\infty^2\sin^2\theta)\chi_{\theta\theta}+\frac{\cos\theta}{\sin\theta}(1-2M_\infty^2\sin^2\theta)\chi_\theta+3C_2q_\infty\cos\theta\left(1-\frac{3}{2}M_\infty^2\sin^2\theta\right)=0 \tag{27a}$$

$$\xi=1 \quad \chi_{\theta\theta}+C_2q_\infty\cos\theta=0 \tag{27b}$$

The bounded solutions to these equations satisfying the boundary conditions $\chi_\theta=0$ for $\theta=0$ and π are

$$\xi=0 \quad \chi=\frac{3}{2}C_2q_\infty\cos\theta+\text{const}$$

$$\xi=1 \quad \chi=C_2q_\infty\cos\theta+\text{const} \tag{28}$$

These expressions constitute the two remaining boundary conditions. The constants have no physical importance, implying a finite potential difference between infinitely separated points.

V. Finite Difference Solution

A. General Outline

The potential Eq. (23) is solved by using a finite difference technique of basically the same kind as was introduced by Murman and Cole.[4] It is a successive line-relaxation procedure with a difference algorithm which is different in subsonic and supersonicflow regions. In subsonic regions all the second-order derivatives are formed by using central differences. In supersonic regions the basic principle is to use backward differencing for those second-order derivatives which constitute derivatives in the streamwise direction, while retaining central differences for the rest of the second-order derivatives, thus keeping the proper domain of dependence for the difference equation. When the streamwise direction is not aligned with one coordinate direction this means a so-called rotated difference scheme has to be used in the supersonic regions. The technique used here is based on that of Jameson.[6] A description of it has also been given by South and Jameson.[7]

B. Rotated Scheme

The principal part of the potential Eq. (23) (the terms containing second-order derivatives) is first rewritten in new coor-

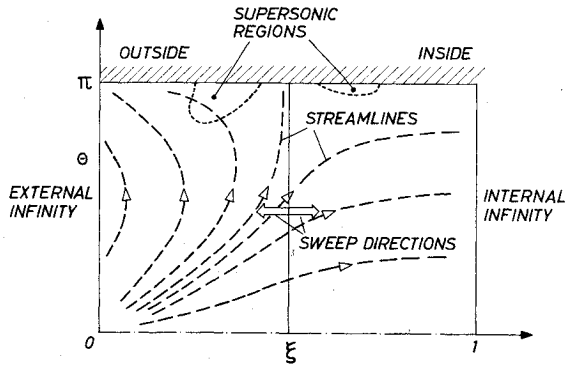

Fig. 7 Sweep directions in the line relaxation procedure.

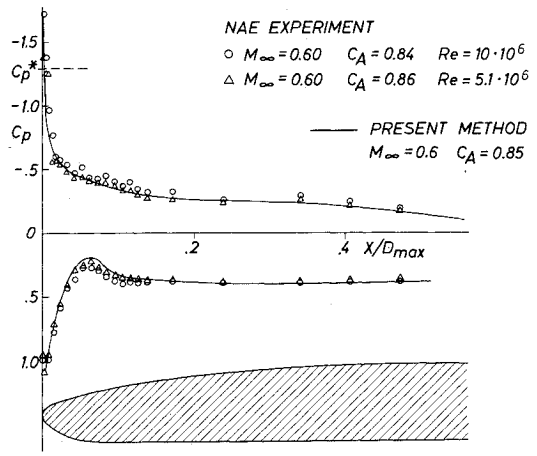

Fig. 8 Pressure distribution around inlet LU-28 at $M_\infty = 0.6$.

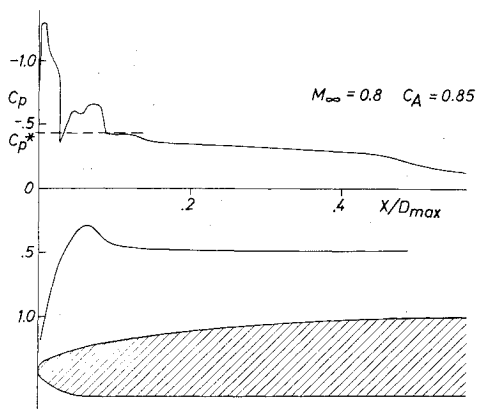

Fig. 9 Pressure distribution around inlet LU-28 at $M_\infty = 0.8$.

dinates chosen to have the same length scale factors. Thus, introducing ξ', θ' by the relations

$$d\xi' = \frac{1}{E(1-\xi)^2}\, d\xi\,, \qquad d\theta' = d\theta$$

with

$$E = 1 - \exp[-\xi/(1-\xi)]$$

the new principal part of Eq. (23) is

$$f(\xi')[(a^2 - q_1^2)\chi_{\xi'\xi'} - 2q_1q_2\chi_{\xi'\theta'} + (a^2 - q_2^2)\chi_{\theta'\theta'}] \tag{29}$$

where $f(\xi')$ denotes a function of ξ'.

If a simple rotational transformation is made to a coordinate system s', n', aligned with and normal to the local velocity vector, it is seen that this expression may be rewritten in the following way

$$f(\xi')\left[\frac{a^2-q^2}{q^2}(q_1^2\chi_{\xi'\xi'} + 2q_1q_2\chi_{\xi'\theta'} + q_2^2\chi_{\theta'\theta'}) + \frac{a^2}{q^2}(q_2^2\chi_{\xi'\xi'} - 2q_1q_2\chi_{\xi'\theta'} + q_1^2\chi_{\theta'\theta'})\right] \tag{30}$$

with $q^2 = q_1^2 + q_2^2$ where, to first order, the terms in the first parenthesis represent $q^2\chi_{s's'}$ and those in the second parenthesis represent $q^2\chi_{n'n'}$.

The principal part (30) is transformed back to the ξ and θ coordinates, and when the difference expressions are formed for the supersonic points the rule followed is to use backward differences (in both the ξ- and θ-direction) for all second-order derivatives in the expression for $\chi_{s's'}$ in Eq. (30) and central differences for the second-order derivatives in the expression for $\chi_{n'n'}$. All first-order derivatives are formed using central differences.

The backward and central difference formulas for the rotated scheme are written with the following restrictions derived by Jameson[6] from a von Neumann stability test

$$\sum_{p,q} c_{pq}^{(n)} = \sum_{p,q} c_{pq}^{(n+1)} = 0 \tag{31}$$

$c_{pq}^{(n)}$ is the coefficient for $\chi_{i+p,j+q}^{(n)}$, i.e., for the potential of iteration level n in the point $\xi = (i+p)\Delta\xi, \theta = (j+q)\Delta\theta$ in a difference formula for the point $\xi = i\Delta\xi$, $\theta = j\Delta\theta$.

C. Solution Procedure

With the rotated scheme used for the supersonic regions the flowfield is successively updated for lines of constant ξ sweeping the field so that, at least in the supersonic regions, the sweep direction will differ at most by 90° from the streamwise direction (see Fig. 7). The line dividing the sweep directions is free of choice, so depending on the mass-flow ratio and Mach number a proper location can always be chosen to satisfy the requirements on sweep direction.

The relaxation factor is equal to 1 in the supersonic regions and chosen between 1 and 2 in the subsonic regions, except near $\xi = 0$ and 1. For these boundary domains it is suitable to underrelax in cases with high subsonic Mach numbers. This depends on the high numerical sensitivity of the difference equation in these regions, which is a consequence of the fact that the potential equation with its boundary conditions tends to an overdetermined problem when ξ tends to 0 and 1. For the limiting equations given in Eq. (27) are ordinary first-order differential equations in χ_θ, which should generally have only one boundary condition on χ_θ.

Instead of underrelaxing, the numerical stability inside the inlet may be improved by replacing one of the Neumann boundary conditions by a total mass-flow condition. The centerline boundary condition was removed and, instead of applying the potential difference equation to mesh points along the centerline, the equation system for a ξ line was closed by applying a total mass-flow difference equation written for the points on that and the upstream ξ line. This technique permits the use of a larger relaxation factor inside the inlet and is included as an option in the program.

As boundary conditions along $\xi = 0$ and $\xi = 1$ the expressions in Eq. (28) with the constant equal to zero for $\xi = 0$ and floating for $\xi = 1$ are used. The solution was found to be rather insensitive to various ways of expressing the boundary

condition for $\xi=1$ through extrapolation from upstream ξ lines.

For high subsonic Mach numbers, where, in some cases, more than one shock wave may exist, high resolution in the pressure field is required, which means that the calculation must be performed on a very fine mesh. This is accomplished in the present program by halving the mesh size in combination with boundary shifting a suitable number of times. The boundaries $\xi_1=0$, $\xi_2=1$, and $\theta_1=0$ may be kept unshifted or shifted to any prescribed new set of values for ξ_1, ξ_2, θ_1 inside the calculated field at the first mesh size halving and so on, freezing the calculated potential on the new boundaries. As may be expected, the most important boundary with respect to the accuracy of the result is the ξ_1 boundary, representing the external infinity when equal to 0. However, comparisons with calculations on grids with refined mesh size and unshifted boundaries have shown that, for a given original grid, a proper sequence of boundary shifts at the mesh halving is easily found, which has hardly any noticeable effect on the accuracy of the inlet pressure distribution.

The required number of iterations on the finer grids is generally smaller than on the coarser ones, although the number of mesh-points usually increases. This is partly due to the favorable effects on the numerical stability of shifting the ξ boundaries away from $\xi=0$ and $\xi=1$ and/or replacing the Neumann condition on $\theta=0$ by a Dirichlet condition for some $\theta\neq 0$.

In the calculations reported following typical dimensions of the initial mesh were 40×20 or 40×30 points along the ξ and θ axis. The finer meshes had up to 96×42 points. Depending upon the number of mesh size halvings, the number of points within each mesh, the Mach number, etc., the computing times ranged from 0.5 to 4 CPU min on a CDC 6600 computer.

VI. Numerical Results

No accurate numerical results were found in the literature for high subsonic Mach number flow around inlets. Thus a number of calculations are presented for cases where experimental results are available. All Reynolds numbers given are based on the maximum external inlet diameter $D_{\max}$.

In Figs. 8-10 pressure distributions are shown around an inlet with the SAAB-SCANIA designation LU-28. Experiments, made at NAE in Canada, were available for $M_\infty=0.6$ and 0.9, showing very good agreement with the calculations.

In Fig. 9 two separate supersonic regions are seen. This calculation was performed using three mesh refinements to get the desired resolution, a number which was rather typical for the calculations presented here.

A different inlet, (denoted LU-3) with an almost elliptical lip form is shown in Fig. 11 in a flow with the same Mach number and mass-flow ratio as in Fig. 10. As expected, the

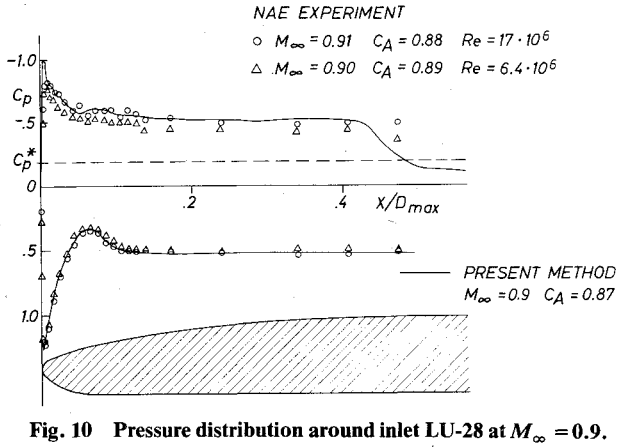

Fig. 10 Pressure distribution around inlet LU-28 at $M_\infty=0.9$.

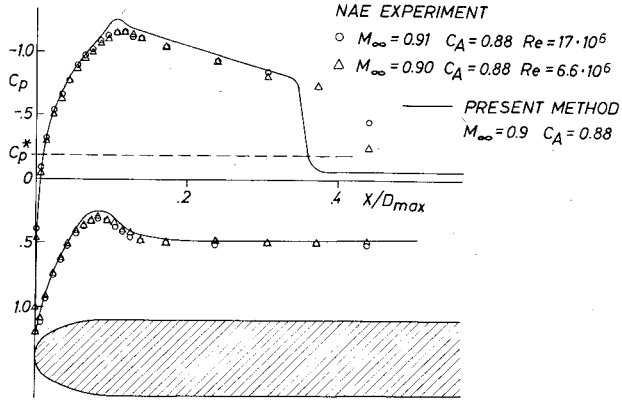

Fig. 11 Pressure distribution around inlet LU-3.

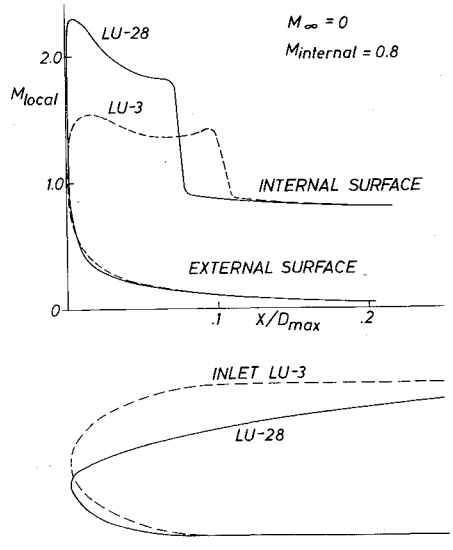

Fig. 12 Static condition. Local Mach number distribution for inlet LU-28 and Lu-3.

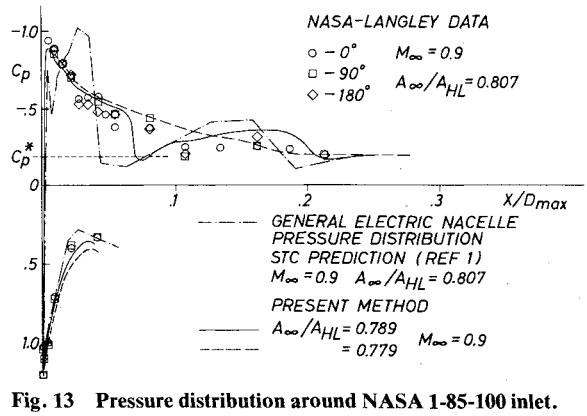

Fig. 13 Pressure distribution around NASA 1-85-100 inlet.

blunt lip of LU-3 yields a much higher suction level and a much stronger shock wave than LU-28. The agreement between experiment and calculations is very good except for the shock wave location, which is predicted slightly upstream of the measured location, a tendency which may be noted also in Fig. 10 for LU-28.

The results of a calculation of LU-28 and LU-3 in a static case are shown in Fig. 12. It is seen that here the blunt-lipped LU-3 has the weakest shock.

A few calculations were made for a NASA 1-85-100 inlet studied by Keith et al,[1] and a result for flow at Mach number 0.9 is shown in Fig. 13. The present method curves are seen to agree quite well with the experimental results, and they also

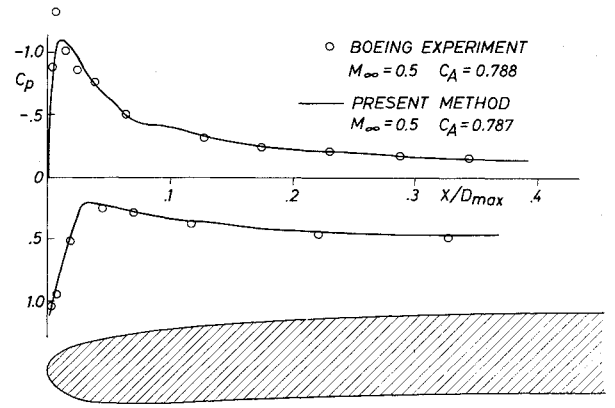

Fig. 14 Pressure distribution around inlet $L_{2\text{-}2}$ at $M_\infty = 0.5$.

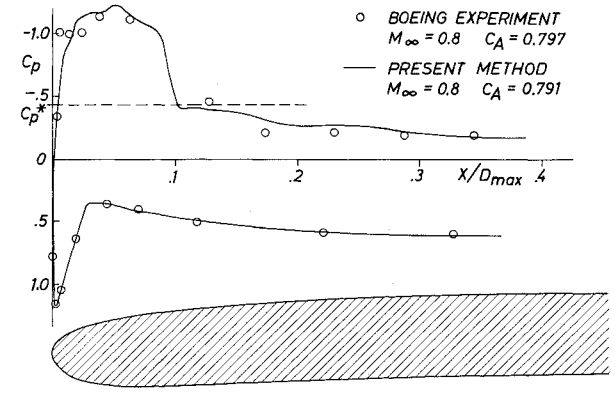

Fig. 15 Pressure distribution around inlet $L_{2\text{-}2}$ at $M_\infty = 0.8$.

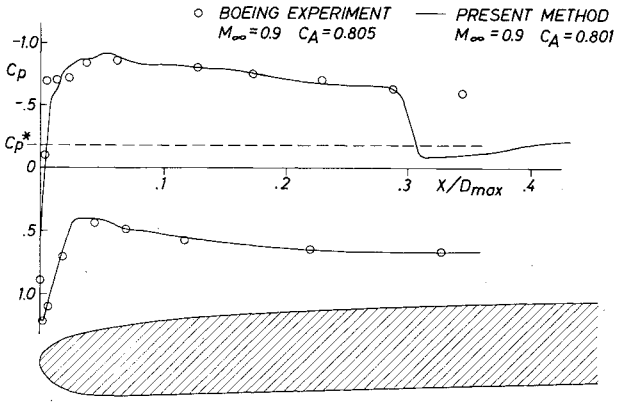

Fig. 16 Pressure distribution around inlet $L_{2\text{-}2}$ at $M_\infty = 0.9$.

illustrate that, in some cases with supersonic regions, the pressure distribution may be rather sensitive to the mass-flow ratio.

In Fig. 14-17 calculated pressure distributions are compared with experimental results obtained by Boeing for an inlet with the Boeing designation $L_{2\text{-}2}$. The Reynolds number, based on the inlet maximum diameter, was about 3.10^6 in these experiments. The agreement between calculations and experiments is seen to be very good for all Mach numbers except for a discrepancy in shock wave location at $M_\infty = 0.9$.

A better comparison between calculated and experimental shock wave locations is seen from Fig. 18, where the calculated supersonic regions are depicted, together with the experimentally observed shock patterns. The latter were taken from rather small figures and should be regarded as somewhat uncertain. However, the observed and the calculated shock waves agree quite well, apart from a small upstream shift in the calculated shocks, which was noted also for LU-3 and LU-28.

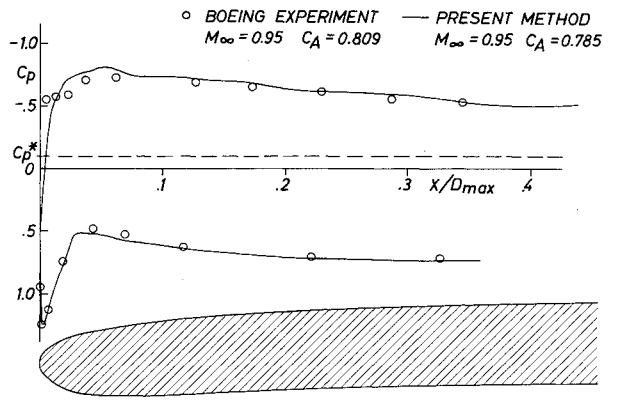

Fig. 17 Pressure distribution around inlet $L_{2\text{-}2}$ at $M_\infty = 0.95$.

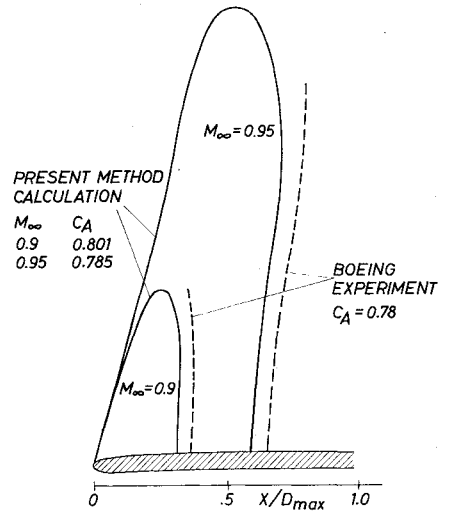

Fig. 18 Supersonic regions outside inlet $L_{2\text{-}2}$ for $M_\infty = 0.9$ and 0.95.

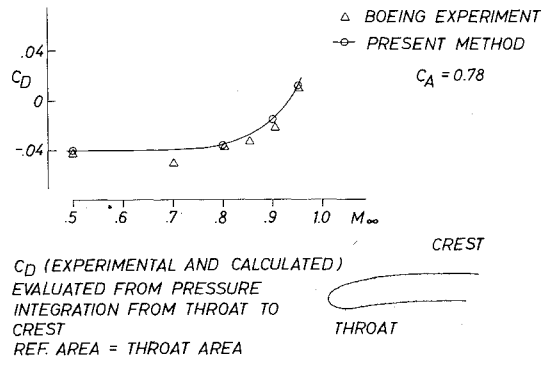

Fig. 19 Drag rise for inlet $L_{2\text{-}2}$.

A similar discrepancy in shock wave location has been noticed by others. Thus Hsieh[8] gets quite analogous results when he compares experiments with the South-Jameson[7] theory for the full potential equation, (see his Fig. 17). One main reason for this discrepancy between theory and experiment is probably the nonconservative formulation of the potential equation. Both Murman[9] and Jameson[10] have noticed that introduction of a fully conservative formulation of the potential equation tends to strengthen the shock and move it aft.

A source of error which will influence results for flows with strong shock waves is the isentropic approximation. Using that means that the discontinuity relations for increasing shock strengths gradually diverge from the correct Rankine-Hugoniot relations, as discussed, for instance, by van der

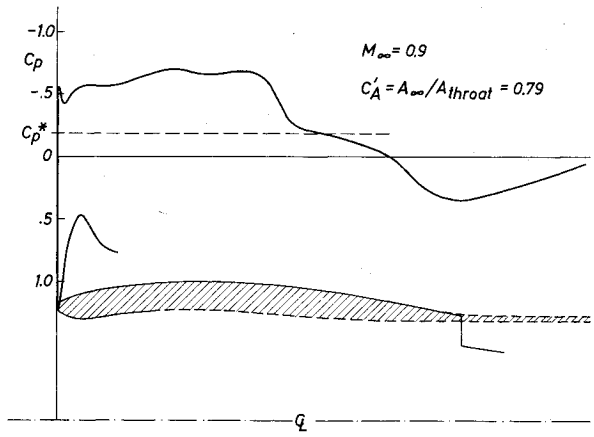

Fig. 20 Pressure distribution on a fan cowl.

Vooren and Slooff[11] and Steger and Baldwin.[12] Also, one should always be aware of the experimental uncertainties due to wind-tunnel-wall interference and viscous effects.

To get a drag coefficient the calculated pressure distributions for the inlet $L_{2\text{-}2}$ were integrated from throat to crest and compared to the corresponding experimental results obtained at Boeing by pressure integration. From the comparison, shown in Fig. 19, it is concluded that the present method is of value when determining the divergence Mach number in cases were no large viscous effects are prevailing.

Figure 20 illustrates how the method may be used for calculating the pressure distribution around a whole continuous surface downstream of the lip region. The contour of a fan cowl and its continuation in a calculation model is sketched, using a simple approximation for the boundary of the fan outflow. The somewhat wavy pressure distribution over the first half of the cowl is due to a corresponding waviness in the curvature distribution of the cowl contour.

VII. Conclusions

A numerical method has been developed for the calculation of the transonic flowfield around an axisymmetric inlet of arbitrary geometry. The full inviscid transonic potential equation is solved in a rectangular calculation plane arrived at by applying conformal mapping to the whole inner and outer flowfield. To get the iterative solution process stable for high subsonic Mach numbers using the line-relaxation technique, a so-called rotated difference scheme had to be used in the supersonic regions. This scheme proved to work quite well and the comparisons between calculated and experimental pressure distributions for Mach numbers 0.5-0.95 show generally very good agreement. A small but consistent discrepancy in shock wave location was found in several cases. The calculation results for high subsonic Mach numbers as well as for static conditions indicate the usefulness of the present method for inlet analysis.

As a further development it would be of value to introduce a conservative formulation of the potential equation to improve the shock jump conditions and also to extend the method to work with supersonic freestream Mach numbers. The important three-dimensional case of an inlet in a flow at angle of attack might be solved by using the same mapping technique as in the present method, but implies a considerable increase in complexity, memory requirements, and running time.

References

[1] Keith, J. S., et al., "Analytical Method for Predicting the Pressure Distribution about a Nacelle at Transonic Speeds," NASA CR-2217, July 1973.

[2] Grossman, B. and Moretti, G., "Development of Analytical Methods of Predicting the Pressure Distribution about a Nacelle at Transonic Speeds-Exact Solution," NASA CR-112271, July 1973.

[3] Colehour, J. L., "Transonic Flow Analysis Using a Streamline Coordinate Transformation Procedure," AIAA Paper 73-657, Palm Springs, Calif., 1973.

[4] Murman, E. M. and Cole, J. D., "Calculation of Plane Steady Transonic Flows," *AIAA Journal*, Vol. 9, Jan. 1971, pp. 114-121.

[5] Jameson, A., "Transonic Flow Calculations for Airfoils and Bodies of Revolution," Aerodynamics Rept. 390-71-1, Grumman Aerospace Corp., 1971 (private communication related to this report).

[6] Jameson, A., "Iterative Solution of Transonic flows over Airfoils and Wings, including Flows at Mach 1," *Communications on Pure and Applied Mathematics,* Vol. 27, 1974, pp. 283-309.

[7] South, J. C. and Jameson, A. "Relaxation Solutions for Inviscid Axisymmetric Transonic Flow over Blunt or Pointed Bodies," *Proceedings from AIAA Computational Fluid Dynamics Conference*, Palm Springs, Calif., pp. 8-17, 1973.

[8] Hsieh, T., "Flowfield Study about a Hemispherical Cylinder in Transonic and Low Supersonic Mach Number Range," AIAA Paper 75-83, Pasadena, Calif., 1975.

[9] Murman, E. M., "Analysis of Embedded Shock Waves Calculated by Relaxation Methods," *Proceedings from AIAA Computational Fluid Dynamics Conference*, Palm Springs, Calif., pp. 27-40, 1973.

[10] Jameson, A., "Transonic Potential Flow Calculations Using Conservation Form," *Proceedings from AIAA 2nd Computational Fluid Dynamics Conference,* Hartford, Conn., pp. 148-161, 1975.

[11] van der Vooren, J. and Slooff, J. W., "On Inviscid Isentropic-Flow Models Used for Finite Difference Calculations of Two-Dimensional Transonic Flows with Embedded Shocks about Airfoils," NLR MP 73024 U, National Aerospace Laboratory, The Netherlands, 1973.

[12] Steger, J. L. and Baldwin, B. S., "Shock Waves and Drag in the Numerical Calculation of Isentropic Transonic Flow," NASA TND-6997, Oct. 1972.